Volume 1 | Number 1 | Jan 2013 | Pages 1–100

Nanoscale

www.rsc.org/nanoscale

ROYAL SOCIETY OF CHEMISTRY

This is an *Accepted Manuscript*, which has been through the Royal Society of Chemistry peer review process and has been accepted for publication.

Accepted Manuscripts are published online shortly after acceptance, before technical editing, formatting and proof reading. Using this free service, authors can make their results available to the community, in citable form, before we publish the edited article. We will replace this *Accepted Manuscript* with the edited and formatted *Advance Article* as soon as it is available.

You can find more information about *Accepted Manuscripts* in the **Information for Authors**.

Please note that technical editing may introduce minor changes to the text and/or graphics, which may alter content. The journal's standard **Terms & Conditions** and the **Ethical guidelines** still apply. In no event shall the Royal Society of Chemistry be held responsible for any errors or omissions in this *Accepted Manuscript* or any consequences arising from the use of any information it contains.

ROYAL SOCIETY OF CHEMISTRY

www.rsc.org/nanoscale

Robust Room Temperature Valley Polarization in Monolayer and Bilayer WS$_2$

Pramoda K. Nayak [1,3‡], Fang-Cheng Lin[2‡], Chao-Hui Yeh[1], Jer-Shing Huang[2*], Po-Wen Chiu[1*]

[1]Department of Electrical Engineering, National Tsing Hua University, Hsinchu 30013, Taiwan

[2]Department of Chemistry, National Tsing Hua University, Hsinchu 30013, Taiwan

[3]Interdisciplinary School of Green Energy and Low Dimensional Carbon Materials Center, Ulsan National Institute of Science and Technology (UNIST), Ulsan 689-798, Republic of Korea

Abstract

We report robust room temperature valley polarization in chemical-vapor-deposition (CVD) grown monolayer and bilayer WS$_2$ via polarization-resolved photoluminescence measurement using excitation below bandgap. We show that excitation with energy slightly below the bandgap of the multi-valleyed transition metal chalcogenides can effectively suppress the random redistribution of excited electrons and, thereby, greatly enhance the efficiency of valley polarization at room temperature. Compared to mechanically exfoliated WS$_2$, our CVD grown WS$_2$ films also show enhancement in the coupling of spin, layer and valley degree of freedom and, therefore, provide improved valley polarization. At room temperature, using below-bandgap excitation and CVD grown monolayer and bilayer WS$_2$, we have reached a record-high valley polarization of 35% and 80%, respectively, exceeding the previously reported values of 10% and 65% for mechanically exfoliated WS$_2$ layers using resonant excitation. This observation provides a new direction to enhance valley control at room temperature.

Keywords: valley polarization, WS$_2$, below-bandgap excitation, chemical vapor deposition, transition metal dichalcogenides

[‡]*These authors contributed equally to this work.*

*Correspondence E-mail; jshuang@mx.nthu.edu.tw or pwchiu@ee.nthu.edu.tw

Introduction

Transition-metal dichalcogenides (TMDs) are known as multi-valley semiconductors with the band-edge located at energy degenerate valleys (±K) at the corners of the hexagonal Brillouin zone.[1-4] As a consequence of degeneracies arising from crystal symmetries, it is possible for electron states to have additional spin-like quantum numbers[5, 6] at band-edges called valleys. The concept of valleytronics is to utilize such valley degree of freedom of electron quantum states and to store the information of 0s and 1s as different discrete values of the momentum space.[5] Besides crystal symmetry, strong spin-orbit coupling originated from the d orbitals of the heavy metal atoms leads to coupled spin and valley physics, making controls of spin and valley possible in these 2D materials.[7,8]

Tungsten disulfide WS_2, is a layered compound with a covalently bonded S-Mo-S hexagonal quasi-two-dimensional network packed by weak van der Waals forces.[2, 9] It shows interesting physical properties due to its nature of crossover from indirect band gap semiconductor (multilayers) to direct band gap semiconductor (monolayer).[10-13] Monolayer WS_2 has drawn great research attention as it exhibits a direct bandgap (~1.98 eV)[11, 13] at the two degenerate valleys, like its sister compound MoS_2. Monolayer WS_2 could be presumably addressed through nonzero orbital magnetic moments and Berry curvatures of the block states that arise from the lack of spatial inversion symmetry.[3, 5, 14, 15] The lack of inversion symmetry in monolayer gives rise to a valley-contrasting optical selection rule,[2, 5, 15-17] where the inter-band transitions in the vicinity of the K (K$'$) point couple exclusively to right (left)-handed circularly polarized light with s = σ+(σ-), as shown in Fig. 1a. The effects of spatial inversion symmetry breaking and giant spin-orbit coupling that arises primarily from the d orbits of tungsten atoms promise monolayer WS_2 to be an ideal system for valleytronics applications.[3,8]

Recently, bilayer WS_2 has drawn attention of the research community of valleytronics[3] because its behavior is dominated not only by the structural symmetry but also the interlayer coupling. Therefore, bilayer WS_2 holds an extra index called layer polarization in addition to the spin and valley degrees of freedom. Such extra index gives information of the location of carriers, either up-layer or down-layer (Fig. 1b). In the case of natural 2H bilayer WS_2, each layer is 180° in plane rotated with respect to the other with the tungsten atoms of a given layer sitting exactly on top of the S atoms of the other layer. For this configuration, the spatial inversion symmetry is recovered. The interlayer coupling is typically strong due to the linear combinations of the d orbital of W atoms and the p orbital of S atoms that have strong interlayer overlap similar to 2H bilayer MoS_2.[18] The rotational symmetry of the layer switches K and K' valleys, but leaves the spin unchanged, which results in the change of sign for the spin-valley coupling from layer to layer (Fig. 1b). Intuitively, one would except that the valley dependent physics becomes less pronounced in bilayers owing to spatial inversion symmetry.[19] However, the inversion symmetry becomes subtle if the coupling of spin, valley, and layer indices is taken into consideration. This opens a new window toward the manipulation of quantum states that manifesting the valley polarization.

One of the most relevant issues for valleytronics is the degree of valley polarization. Typically, resonant excitation is employed in order to obtain maximum emission intensity. However, at room temperature, the valley polarization is greatly limited by random thermal distribution of the excited state electrons. Therefore, low temperature is typically favored for enhancing the valley polarization. In fact, if the excitation energy is much larger than the resonant energy, the valley polarization can also be suppressed by the non-radiative relaxation of the over excited electrons (i.e. hot electrons).[17] In this work, we demonstrate robust and enhanced room-temperature valley polarization of monolayer and bilayer WS_2 in polarization-resolved photoluminescence (PL)

experiment by using excitation energy slightly below the direct bandgap of WS_2. Unlike the commonly used resonant excitation, excitation below the bandgap can greatly suppress the loss of the valley polarization due to the thermally induced inter-valley redistribution and non-radiative relaxation of the excited electrons. We show greatly improved valley polarization of ~35 % and ~80% for monolayer and bilayer WS_2, in comparison with the highest reported values of 10% and 65 % for monolayer and bilayer WS_2, respectively.

Results and Discussion

Single crystals of WS_2 islands with variable thickness were synthesized directly on silicon substrates by chemical vapor deposition (CVD) as reported in our previous work[13] and their surface morphology can be found in Fig. S1 & Fig. S2 (Supporting Information). Under white light illumination, the color contrast due to light interference through the sample and thin dielectric layer gives a clear indication of the film thickness as indicated by marked regions in Fig. S1. The layer assignment was doubly confirmed by atomic force microscopy (AFM) (see Supporting Information, Fig. S3). Out of all the WS_2 islands, we have chosen the monolayer and bilayer regions for the valley polarization measurement. Fig. 2a shows the PL mapping images of monolayer and bilayer WS_2 obtained using CW He-Ne laser excitation at 633 nm. The PL intensity is high and homogeneous over the area of monolayer WS_2 but the intensity drops within the bilayer region due to the increase in layer thickness. The angle between the lattices of the top layer and the bottom layer is $0°$. Here, we have chosen such kind of bilayers with $0°$ twist angle and full overlapping region. More examples of $0°$ twist angle bilayers can be found in Fig. S1b (Supporting Information)

Raman spectroscopy is a fast, nondestructive and unambiguous way to identify the thickness of layered materials.[20-22] Room-temperature Raman spectra of monolayer and bilayer WS_2 islands

acquired with 633-nm laser excitation are shown in Fig. 2b. The number of WS$_2$ layer is revealed by the intensity ratio of the two characteristic Raman primary modes: the in-plane vibrational mode (E_{2g}^1) observed at 353.9 cm^{-1} and the out-of-plane vibrational mode (A_{1g}) at 418.2 cm^{-1}.[23] The ratio of E_{2g}^1 / A_{1g} peak intensity is 0.75 for monolayer and increases to 0.95 for bilayer WS$_2$, which is close to the value observed by Berkdemir *et al.* [22] with 647-nm laser excitation. As for the intensive peak at 520.6 cm^{-1} and weak peak around 383 cm^{-1}, they correspond to the Si substrate and the multi-phonon combinations of these primary modes, respectively.

For quantum manipulations in atomically thin TMD systems, coherence of electronic states is crucial. Such coherence can be achieved under cryogenic temperatures[2,3,24,25] mainly because the random thermal distribution of electrons is effectively minimized. However, such low temperature limits practical applications of TMD. Therefore, to achieve room-temperature coherent state in dichalcogenide systems is of great research interest. Since the degree of coherence is reflected by the valley polarization of the dichalcogenide systems, we have measured room-temperature valley polarization in monolayer and bilayer WS$_2$ with polarization-resolved photoluminescence measurements in order to understand the system coherence. A homemade confocal microscopic setup has been used for the polarization-resolved PL measurement. The PL with total intensity (I) is collimated and aligned into a broadband λ/4 wave plate such that right-(σ+) and left-handed (σ−) circularly polarized emission are converted into two orthogonally polarized components with intensity I+ and I−. The two orthogonal polarization components are then separated by a polarization beam splitter (BS) and focused onto the entrance slit of the monochromator equipped with a charge-coupled device camera (CCD, DU401A-BV, Andor). The polarization resolved spectrum is then obtained by analyzing the two branches of dispersion on the CCD. Please see Fig. S4 (Supporting Information) for the details of the optical setup.

Fig. 2c and 2d present the photoluminescence spectra from monolayer WS_2 measured at 300 K under illumination of circularly polarized laser excitation 633 nm (1.96 eV). The energy range between 1.94 and 2.00 eV is removed for clarity because the laser background seriously overlaps with the sample emission in this spectral region. The peaks in the PL spectra for monolayer WS_2 are dominated by the emission from band-edge "A" excitons at K and K′ valleys, corresponding to the left- and right-handed circularly polarized emission. The excitons carry a clear circular dichroism under near- but below-bandgap excitation (1.96 eV) with circular polarization, which is a result of valley-selective optical selection rules.[2,5,15,17] The PL follows the helicity of the circularly polarized excitation optical field as clearly observed from Fig. 2c & 2d. In the case of right-handed circularly polarized excitation (σ+) (Fig. 2c), the intensity of the beam (I+) is larger compared to horizontal component (I−), whereas the horizontal component exceeds the vertical one in the case of left-handed circularly polarized excitation (σ−) (Fig. 2d). The degree of circular polarization of the emission, reflecting the efficiency of valley polarization, has been calculated using the following relation,[2,17,19]

$$\eta = \frac{PL(I+) - PL(I-)}{PL(I+) + PL(I-)}, \tag{1}$$

where (I+) and (I−) are the intensity of the two orthogonally polarized components, corresponding to the right- (σ+) and left-handed (σ−) circularly polarized emission. Fig. 3a displays a contrasting polarization obtained using circularly polarized 633 nm excitation with opposite handedness. We have obtained η = +35±3% under σ+ excitation and η = −35±3% under σ− excitation at 300 K. This value is quite large compared to the reported results using resonant excitation on monolayer WS_2 (~10%)[3] and MoS_2 (~0%)[2,17] at room temperature. To double check the result, same measurement has been repeated on a different monolayer region. Again, very high polarization efficiency around +37±3% and −37±3% are obtained for σ+ and σ− excitation, respectively,

confirming the robustness of below-bandgap excitation method (Fig. S5, Supporting Information).

The robust and very high valley polarization at room temperature can be attributed to the following

two factors. One is the choice of the growth substrate and the other one is the improved selective

valley excitation using near- but below-bandgap excitation. The valley polarization efficiency

greatly concerns with the intervalley scattering and the exciton lifetime, which are strongly

substrate dependent. For example, the PL quantum yield of MoS_2 grown on *h*-BN is large than that

on SiO_2/Si substrate.[17] Similarly, the PL quantum yield of MoS_2 on SiO_2/Si is larger than that on

sapphire substrate.[26] In the present work, the substrate is 300-nm thick SiO_2/Si, which has higher

surface roughness (300 pm) than the sapphire substrate (50 pm), as can be seen in Fig. S6

(Supporting Information). Therefore, WS_2 layers grown on a 300-nm thick SiO_2/Si substrate have

relatively large non-radiative decay rate and lower emission quantum yield compared to that on

sapphire substrate. The weaker emission partially accounts for the relatively large circular

polarization, as reported by Wu *et al.*[26] The second factor is the selective valley excitation, which

is crucial to the fidelity of valley polarization at 300 K.[27] Intuitively, resonant excitation should be

ideal for selective valley excitation, *i.e.* initial excitation energy equal to the bandgap. However,

at room temperature, intervalley scattering can be significantly increased due to enhanced phonon

populations,[5] resulting in the decrease in the valley polarization. Therefore, at room temperature,

resonant excitation might not provide the best valley selectivity. Instead of resonant excitation,

using excitation with energy near but slightly below the bandgap can effectively reduce the

intervalley scattering and, thereby, enhance the valley polarization. The price to pay is the decrease

of the emission intensity. We note that if the initial excitation energy is too much higher or lower

than the bandgap, Fermi-Golden rule is not strictly followed and the valley polarization can no

longer be observable (inset of Fig. 3a).[28] In the present case, the photon energy of the 633 nm laser

(1.96 eV) is just slightly below the bandgap of the monolayer WS_2 (1.98 eV). As shown in Fig. 3a, the polarization efficiency of the PL is greatly enhanced with below-bandgap excitation, at a slight sacrifice in the emission intensity. Such enhancement in the valley polarization can be further explained by the following model depicted in Fig. 3b.

In multi-valleyed semiconductors like TMDs, the valley selection rule is valid in the vicinity of the K (K′) point.[5,16] When the excitation energy is slightly lower than that of energy of ground state of exciton (within the range of band width, Fig. 3b left panel), the electrons are not able to move from valance band to conduction band because the excitation energy is insufficient and instead travel up to metastable energy state marked as orange line in Fig.3b (right panel). However, if the phonon population is very large near the band edge, as at room temperature, phonons can provide energy to the electrons in the vicinity of conduction band edge and thereby promote the electrons up to the conduction band marked as red arrows. The electrons in the conduction band and holes in the valence band undergo non-radiative relaxation (black arrows) due to phonon assistance and recombine to form exciton thereby releasing energy in the form of photon. In such an excitation process, the intervalley scattering due to phonons at room temperature is effectively minimized and the valley polarization is enhanced. Of course, the intensity of the photoluminescence is not as high as that obtained with resonant excitation[3] or excitation with energy higher than the bandgap.[2, 17] Using slightly below-bandgap excitation, the large population of phonons at room temperature indeed promotes the valley selective excitation instead of intervalley scattering as in the case of resonant excitation, leading to enhanced valley polarization efficiency.

Next, we perform same polarization measurement on bilayer WS_2. The results are shown in Fig. 4. Similar to monolayer WS_2, the PL spectra of bilayer WS_2 exhibits A peak (inside the cut off

region), which corresponds to the excitonic emission from direct band transition at K and K′ valleys. Compared to monolayer WS$_2$, the bilayer WS$_2$ exhibits higher PL intensity as well as larger intensity contrasts. This is because the indirect band gap of bilayer WS$_2$ has a lower value of 1.96 eV than the monolayer one. Therefore, the 633 nm laser (1.96 eV) now becomes a resonant excitation source. The PL spectrum in the region of indirect band gap transition I is not plotted here as the emission originating from indirect band gap is unpolarized.[3] There is large intensity variation between the two components (vertical, I+ & horizontal, I–) for right-handed circularly polarized excitation (σ+) and left-handed circularly polarized excitation (σ–). The efficiency of polarization is calculated to be 80±3%, which is higher than the 60 % reported by Zhu *et al.*[3] at room temperature and the PL follows the same helicity of the circularly polarized excitation (Fig. 5a). Similarly, the polarization efficiency measured on another bilayer region comes out to be 78±3% (Fig. S5, Supporting Information). In the following, we discuss and give tentative explanation on the observation of such high valley polarization for bilayer WS$_2$ at room temperature.

In order to exclude the potential cause of charge trapping or substrate charging effect in bilayer WS$_2$, Zhu *et al.*[3] have studied polarization-resolved PL by applying an out of plane electric field and found that the degree of circular polarization remains unchanged for different bias conditions. Hence, the effects of Coulomb screening, charge traps, or charge transfers with substrates can be ruled out to be the major causes for the robust circular dichroism in bilayers against monolayers. One of the potential causes may be the shorter lifetime of excitons at K (K′) valley for bilayer system. The lifetime has been calculated using the following polarization equation,[3, 29]

$$P = \frac{p_0}{1 + \frac{2\tau}{\tau_k}},$$ (2)

where P is the efficiency of circular polarization, p_0 is the theoretical limit of polarization and τ_k and τ denote the valley lifetime and exciton lifetime, respectively. According to equation 2, valley polarization efficiency can be increased if the ratio of τ/τ_k is reduced. Therefore, reducing exciton lifetime (τ) and increasing valley lifetime (τ_k) can lead to the enhancement in valley polarization. To understand which of the two factors plays a major role here, we have performed calculation based on experimental data to estimate the exciton lifetime in our monolayer and bilayer systems. Using P and p_0 values of 0.8 and 1.0, respectively, the exitonic lifetime of our bilayer WS_2 system has been estimated to be 4 ps for corresponding carrier lifetime of 34 ps obtained from time-resolved pump-probe reflectance experiments.[3] In the case of monolayer WS_2, the exitonic life time is found to be 41 ps for the carrier life time of 45 ps. So, the difference in the valley lifetime for monolayer and bilayer system is not as pronounced as the difference in the exciton lifetime. Recently, Yuan *et al.*[30] has predicted exciton life time of bilayer WS_2 to be 401 ps, which is much smaller than that of monolayer (806 ps) from time-resolved photoluminescence (TRPL) spectroscopy under ambient conditions and at room temperature. The calculated exciton life times of monolayer and bilayer WS_2 reported so far are summarized in Fig.5b. Although the absolute values of exciton life time varies reported by several groups due to different samples and measurement conditions, but the trend (i.e. shorter excitonic life time of bilayer compared to monolayer) is same for all the cases. Therefore, this consistency indicates that the difference in excitonic life time is one of the factors behind anomalous valley polarization in bilayer.

From equation 2, τ_k represents the intrinsic radiative decay of excitons and it is strange to notice that the intrinsic radiative decay in bilayer WS_2 is significantly faster than that of monolayer

(Figure 5b). However, this concept is still under debate, as Shi *et al.*[31] observed that non radiative rather than radiative relaxation path ways dominate in mono to few layer TMDs from their transient absorption measurement on both the suspended and substrate supported samples. Moreover, Yuan *et al.*[30] reported that the non-radiative processes dominate the exciton decay and the life time decreases as the number of layer increases. In the present case, PL from monolayer WS_2 by application of low band gap excitation is most likely non-radiative decay process due to need of phonon assistance (Figure 3b) and PL from bilayer WS_2 is also a non-radiative decay process.[30] Hence, it is reasonable that exitonic life time of bilayer is smaller than that of monolayer in the present case, which is partially responsible for large valley polarization in bilayer system.

In bilayers, the depolarization could be either via interlayer hopping, which requires spin flip, or via K $\leftrightarrow$ K' intervalley scattering within the layer in a similar way as in monolayer systems. However, the interlayer hopping at K valley is suppressed in WS_2 due to strong spin-orbital coupling and spin-layer-valley coupling, which have been experimentally proved by the circular dichroism in PL from bilayers.[18] The robust polarization in bilayers implies that the intervalley scattering within a layer is diminished compared to that in monolayers. Exciton binding energy might be another possible direction to be considered in order to explain the higher valley polarization in the bilayer system. Recently, Zhu *et al.*[32] has reported the exciton binding energy of monolayer WS_2 to be 0.71 eV around K-valley in the Brillouin zone using two-photon photoluminescence excitation spectroscopy (TP-PLE). Such a large binding energy of monolayer WS_2 compared to bulk TMDs,[33] whose binding energy is typically tens of meV, comes from the large effective masses of both electrons and holes, the spatial confinement in the out-of-plane direction and the reduced screening of the dielectric environment.[29, 34] However, all these effects are relatively insignificant in bilayer WS_2 compared to monolayer one. In fact, the binding energy

11

of excitons around K valley in bilayer WS_2 is similar to or even slightly smaller than that in monolayer WS_2. Therefore, large excitonic binding energy can be ruled out. Another possible contribution is the extra spin-conserving channels via intermediate intervalley-interlayer scatterings in bilayer WS_2, which are absent in monolayers.[35] The extra spin-conserving channel may compete with the spin-flip process and reduce the relative weight of spin-flip intervalley scattering.

Recently, Liu *et al.*[36] predicts the intrinsic circular polarization in centrosymmetric stacks (n=even) TMDs using first-principles calculations. Bilayer WS_2 is supposed to show highest valley polarization of 93 % than other bilayer TMD system due to large spin orbit coupling (SOC) of W atom and higher PL quantum yield. The intrinsic polarization in centrosymmetric bilayer system originates from the hidden spin polarization that is localized on each WS_2 layer. Finally, there is no doubt that selective valley excitation contributes to large extent for robust polarization like monolayer. So far, the mechanism for the improved valley polarization is still not fully understood and requires further study. Overall, the robust circular polarization in bilayers can possibly stem from combined effects of shorter exciton lifetime, smaller exciton-binding energy, extra spin-conserving channels, coupling of spin, layer, and valley degrees of freedom, local spin polarization and selective valley excitation.

Experimental

CVD Synthesis of WS$_2$

Mono to few layers WS$_2$ flakes were prepared on 300 nm SiO$_2$/Si substrates using low pressure chemical vapor deposition. The detail growth procedure comprising of two-step process, which has been described in our earlier report.[13] In the first step, the WO$_3$ precursor powder was thermally evaporated and deposited on pre-cleaned Si-wafers, with various thicknesses in the range of 10-25 nm. Subsequently, the films were transferred into a quartz tube reactor for sulfurization in the second step. During the sulphurization of WO$_3$ films, a boat with 0.3 g of S powder (99.9 % purity, Alfa Aeser) was kept upstream inside the quartz tube but outside the furnace. This zone was wrapped with an independently controlled thermal-coil, which was heated to a temperature of ~220°C. The WO$_3$ films were heated to 850°C for 30 min under an Ar flow of 100 sccm and a slight hydrogen treatment below 10 sccm at low pressure (30 torr), and react with S vapor to form WS$_2$ platelets, where the reactive zone is allowed at the temperature gradient region around 650-800°C to synthesize mono- to few-layer WS$_2$ flakes (Fig. S1, Supporting Information). Only monolayer and bilayer flakes were selected for polarization measurement.

Room temperature polarization measurement

The polarization-resolved photoluminescence measurement was carried out at room temperature using a homemade confocal-like microscopic set-up (supplementary Fig. S4). The collimated backscattering light (I) was passed through first polarizer P$_1$ (LPVIS100-MP, Thorlabs) followed by a broadband $\lambda/4_1$ wave plate (AQWP05M-600, Thorlabs), where it beam becomes circularly polarized. This circularly polarized beam is being passed through a beam splitter (BS, BS010, Thorlabs) before expose to the sample. The BS separates the light beam into two orthogonally polarized components (I+,I–) followed by another quarter wave plate ($\lambda/4_2$), polarizer (P$_2$) and a

Nanoscale Accepted Manuscript

depolarizer, and was then focused at the entrance slit of the monochromator equipped with a charge-coupled device (CCD, DU401A-BV, Andor) camera. The + or − signal (parallel or perpendicular between two polarizer) is determined by the second polarizer. The polarization resolved spectrum could then be obtained by analyzing the two branches of dispersion on the CCD.

Conclusions

In summary, we have demonstrated anomalously robust room temperature valley polarization ~35 % and ~80 % in CVD grown monolayer and bilayer WS_2, respectively. Slightly below-bandgap excitation can effectively increase the valley polarization efficiency of monolayer WS_2. Selective valley excitation is the major cause for robust valley polarization in monolayer WS_2, whereas the combined effects of the shorter exciton lifetime, smaller exciton-binding energy, extra spin-conserving channels, coupling of spin, layer, and valley degrees of freedom, local spin polarization and selective valley excitation is responsible for large polarization in bilayer WS_2. This observation provides a new direction to enhance valley control via valley selective excitation and creates an intriguing platform for spin and valley physics.

Supporting Information

Additional characterizations including OM, SEM, AFM, experimental set up for polarization measurement, polarization spectra of additional monolayer and bilayer WS_2 flakes, and surface roughness of growth substrates are given in Fig. S1-S6. This material is available free of charge from the Royal Society of Chemistry (RSC) online library or from the author.

Acknowledgements

Notes and references

1. K. F. Mak, C. Lee, J. Hone, J. Shan and T. F. Heinz, *Phys. Rev. Lett.*, 2010, **105**, 136805.

2. H. L. Zeng, J. F. Dai, W. Yao, D. Xiao and X. D. Cui, *Nat Nanotechnol*, 2012, **7**, 490-493.

3. B. R. Zhu, H. L. Zeng, J. F. Dai, Z. R. Gong and X. D. Cui, *P. Natl. Acad. Sci. USA*, 2014, **111**, 11606-11611.

4. N. Kumar, J. Q. He, D. W. He, Y. S. Wang and H. Zhao, *Nanoscale*, 2014, **6**, 12690-12695.

5. D. Xiao, G. B. Liu, W. X. Feng, X. D. Xu and W. Yao, *Phys. Rev. Lett.*, 2012, **108**. 196802.

6. Z. W. Zhu, A. Collaudin, B. Fauque, W. Kang and K. Behnia, *Nat. Phys.*, 2012, **8**, 89-94.

7. Z. Y. Zhu, Y. C. Cheng and U. Schwingenschlogl, *Phys. Rev. B*, 2011, **84**, 153402.

8. H. Zeng, G. B. Liu, J. Dai. Y. Yan, B. Zhu, R. He, L. Xie, S. Xu, X. Chen, W. Yao and X. Cui, *Sci. Rep.*, 2013, **3,** 1608.

9. M. Chhowalla, H. S. Shin, G. Eda, L. J. Li, K. P. Loh and H. Zhang, *Nat. Chem.*, 2013, **5**, 263-275.

10. A. L. Elias, N. Perea-Lopez, A. Castro-Beltran, A. Berkdemir, R. T. Lv, S. M. Feng, A. D. Long, T. Hayashi, Y. A. Kim, M. Endo, H. R. Gutierrez, N. R. Pradhan, L. Balicas, T. E. M. Houk, F. Lopez-Urias, H. Terrones and M. Terrones, *Acs Nano*, 2013, **7**, 5235-5242.

11. H. R. Gutierrez, N. Perea-Lopez, A. L. Elias, A. Berkdemir, B. Wang, R. Lv, F. Lopez-Urias, V. H. Crespi, H. Terrones and M. Terrones, *Nano Lett*, 2013, **13**, 3447-3454.

12. S. Z. Butler, S. M. Hollen, L. Y. Cao, Y. Cui, J. A. Gupta, H. R. Gutierrez, T. F. Heinz, S. S. Hong, J. X. Huang, A. F. Ismach, E. Johnston-Halperin, M. Kuno, V. V. Plashnitsa, R. D. Robinson, R. S. Ruoff, S. Salahuddin, J. Shan, L. Shi, M. G. Spencer, M. Terrones, W. Windl

and J. E. Goldberger, *Acs Nano*, 2013, **7**, 2898-2926.

13. P. K. Nayak, C. H. Yeh, Y. C. Chen and P. W. Chiu, *Acs Appl. Mater. Inter.*, 2014, **6**, 16020-16026.

14. D. Xiao, M. C. Chang and Q. Niu, *Rev. Mod. Phys.*, 2010, **82**, 1959-2007.

15. T. Cao, G. Wang, W. P. Han, H. Q. Ye, C. R. Zhu, J. R. Shi, Q. Niu, P. H. Tan, E. Wang, B. L. Liu and J. Feng, *Nat. Commun.*, 2012, **3**, 887.

16. W. Yao, D. Xiao and Q. Niu, *Phys. Rev. B*, 2008, **77**, 235406.

17. K. F. Mak, K. L. He, J. Shan and T. F. Heinz, *Nat. Nanotechnol.*, 2012, **7**, 494-498.

18. T. Jiang, H. R. Liu, D. Huang, S. Zhang, Y. G. Li, X. G. Gong, Y. R. Shen, W. T. Liu and S. W. Wu, *Nat. Nanotechnol.*, 2014, **9**, 825-829.

19. S. F. Wu, J. S. Ross, G. B. Liu, G. Aivazian, A. Jones, Z. Y. Fei, W. G. Zhu, D. Xiao, W. Yao, D. Cobden and X. D. Xu, *Nat. Phys.*, 2013, **9**, 149-153.

20. C. Lee, H. Yan, L. E. Brus, T. F. Heinz, J. Hone and S. Ryu, *Acs Nano*, 2010, **4**, 2695-2700.

21. S. Najmaei, Z. Liu, P. M. Ajayan and J. Lou, *Appl. Phys. Lett.*, 2012, **100**. 013106.

22. A. Berkdemir, H. R. Gutierrez, A. R. Botello-Mendez, N. Perea-Lopez, A. L. Elias, C. I. Chia, B. Wang, V. H. Crespi, F. Lopez-Urias, J. C. Charlier, H. Terrones and M. Terrones, *Sci, Rep.,* 2013, **3**, 1755.

23. H. S. S. Ramakrishna Matte, A. Gomathi, A. K. Manna, J. Dattatray, R. Datta, S. K. Pati, C. N. R. Rao, *Angew. Chem.,* 2010**, 49***, 4059--4062.

24. A. Jones, H. Yu, N. Ghimire, S. Wu, G. Aivazian, J. Ross, B. Zhao, J. Yan, D. G. Mandrus, D. Xiao, W. Yao, X. Xu, *Nat. Nanotech.,* 2013**, 8***, 634–638.

25. A. Singh, G. Moody, S. Wu, Y. Wu, N. J. Ghimire, J. Yan, D. G. Mandrus, X. Xu, X. Li, *Phys. Rev. Lett.,* 2014**, 112,** 216804.

26. S. Wu, C. Huang, G. Aivazian, J. S. Ross, D. H. Cobden, X. Xu, *ACS Nano,* 2013, **7,** 2768-2772.

27. G. Sallen, L. Bouet, X. Marie, G. Wang, C. R. Zhu, W. P. Han, Y. Lu, P. H. Tan, T. Amand, B. L. Liu, B. Urbaszek, *Phys. Rev. B,* 2012, **86,** 081301.

28. P. A. M. Dirac, Proc. Roy. Soc. A, 1927, **114,** 243-265.

29. H. Y. Yu, X. D. Cui, X. D. Xu, W. Yao, *Natl. Sci. Rev.,* 2015, **2,** 57-70.

30. L. Yuan, L. Huang, *Nanoscale*, 2015, **7,** 7402-7408.

31. H. Shi, R. Yan, S. Bertolazzi, J. Brivio, B. Gao, A. Kis, D. Jena, H. G. Xing, L. Huang, *ACS Nano,* 2013, **7,** 1072−1080.

32. B. R. Zhu, X. Chen, X. D. Cui, *Sci. Rep.,* 2015, **5,** 9218.

33. A. R. Beal, J. C. Knights, W. Y. Liang, *J. Phys. C: Solid State Phys.,* 1972, **5,** 3540-3551.

34. M. Dvorak, S. H. Wei, Z. G. Wu, *Phys. Rev. Lett.,* 2013, **110,** 016402.

35. Y. Song, H. Dery, *Phys. Rev. Lett.,* 2013, **111,** 026601.

36. Q. Liu, X. Zhang, A. Zunger, *Phys. Rev. Lett.,* 2015, **114**, 087402.

Figure Captions

Fig. 1 a) The unit cell of monolayer WS_2 with structural inversion asymmetry. The bottom panel shows the schematic illustration of valley-contrasting circular dichroism when inversion symmetry is broken. (b) spin–layer–valley coupling in 2H stacked bilayer WS_2, which exhibits inversion symmetry. Cartoon in the bottom panel depicting excitation/emission processes in the K valley of bilayer WS_2. Spin configurations indicated by (⇑) and (↑) are for holes and electrons, respectively.

Fig. 2 a) PL intensity mapping of monolayer and bilayer WS_2 using 633 nm laser excitation. For monolayer WS_2, the photoluminescence (PL) is bright and homogeneous throughout the whole surface. In the bilayer region (indicated by an arrow), the intensity becomes relatively low. The

region surrounding the periphery of the grains (WS$_2$-Silicon interface) also shows low PL intensity. The angle between the top layer (reduced intensity) with respect to the bottom layer (large intensity) is 0°. (b) Characteristic Raman spectra from different WS$_2$ flakes (monolayer and bilayer) using 633nm laser excitation. The in-plane vibrational E_{2g}^1 mode and an out-of-plane vibrational A_{1g} mode along with Si peak positions are labeled at 353.9, 418.2 and 520.6 cm^{-1}, respectively. The ratio of E_{2g}^1 / A_{1g} peak intensity is 0.75 for monolayer and increases to 0.95 for bilayer WS$_2$. (c,d) Photoluminescence spectra of monolayer WS$_2$ with right- (σ+) and left-handed circularly polarizations (σ−) using 633 nm near-resonant excitation at 300 K. The PL region in the energy range (1.94 to 2.00 eV) containing intermixing signal of both sample and laser is shown here as cut off for clarity. (I+, I−) are the vertical and horizontal components of the polarized beam respectively.

Fig. 3 a) Polarization resolved luminescence spectra with σ+ detection and σ− detection under near-resonant excitation (1.96eV) at 300 K. The degree of contrasting circular polarizations (polarization efficiency) of η = +35±3% and −35±3% are observed along the out-of-plane direction with right- handed (σ+) and left-handed (σ−) circular excitation, respectively. The PL follows the same helicity of the circularly polarized excitation. The inset shows the polarization spectra for far-resonant excitation (2.33 eV), where no polarization is detected. (b) The schematics showing the condition for valley polarization. The band width of laser excitation falls within the range of emission band width to satisfy ideal condition for polarization. The right panel presents a model explaining possibility of valley polarization even with lower resonant excitation. The red arrows correspond to phonon vibration near the band edge and the orange line refers to a metastable energy state below the conduction band up to which electrons can move by application of slightly below band gap excitation energy. The black arrows present non-radiative relaxation pathways of

electrons and holes. At 300 K, the phonon population is very large near the band edge, which pick up the electrons in the vicinity of conduction band and helps in forming exciton (e^--h^+ pair) via non-radiative relaxation pathways, thereby producing photoluminescence.

Fig. 4 Room temperature photoluminescence spectra from bilayer WS_2 for (a) right-handed circular excitation ($\sigma+$) and (b) left-handed circular excitation ($\sigma-$) using near-resonant (1.96 eV) excitation. The PL region in the energy range (1.94 to 2.00 eV) containing intermixing signal of both sample and laser is shown here as cut off for clarity. ($I+$, $I-$) correspond to vertical and horizontal components of the polarized beam.

Fig. 5 a) Circularly polarized luminescence spectra from bilayer WS_2 with $\sigma+$ detection and $\sigma-$ detection under near-resonant excitation (1.96 eV) at 300K. The degree of contrasting circular polarizations (polarization efficiency) of $\eta = +80\pm3\%$ and $-80\pm3\%$ are observed along the out-of-plane direction with right- handed ($\sigma+$) and left-handed ($\sigma-$) circular excitation, respectively. The PL follows the same helicity of the circularly polarized excitation. (b) Exciton life time for monolayer and bilayer WS_2 reported so far including this work. In all the cases, exciton life time of bilayers is smaller than those of monolayers.
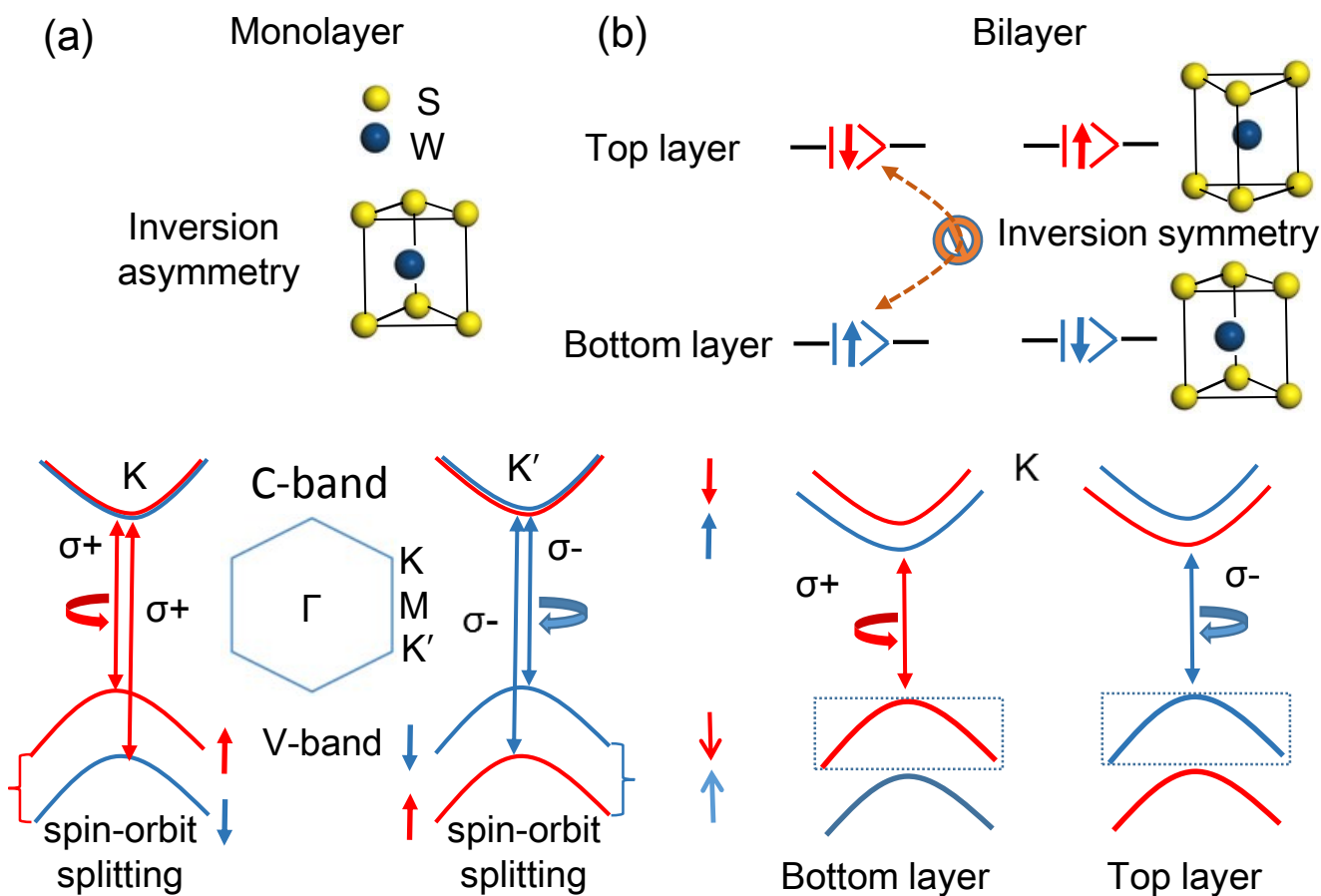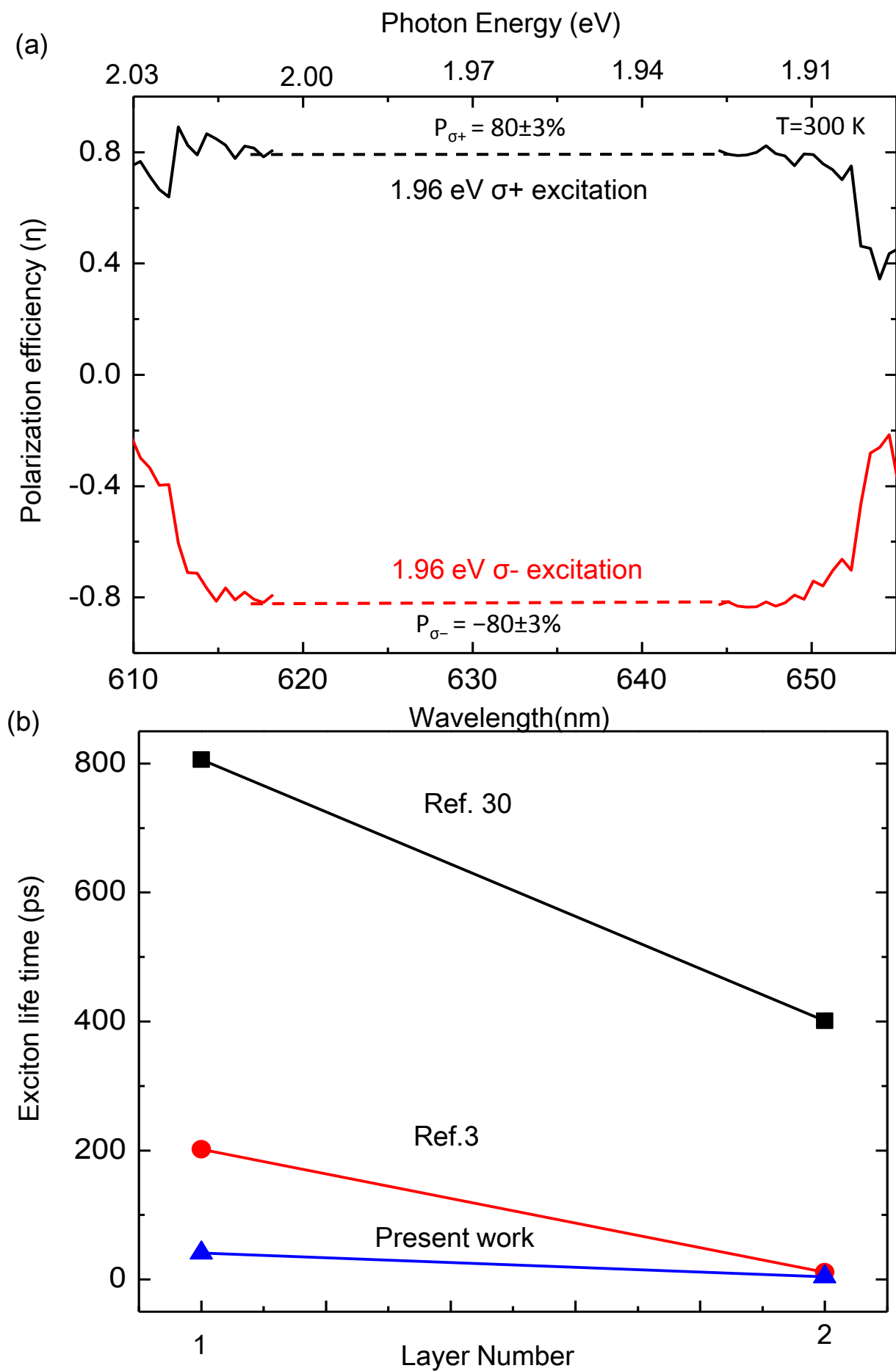
Figure 1 P. K. Nayak *et al.*
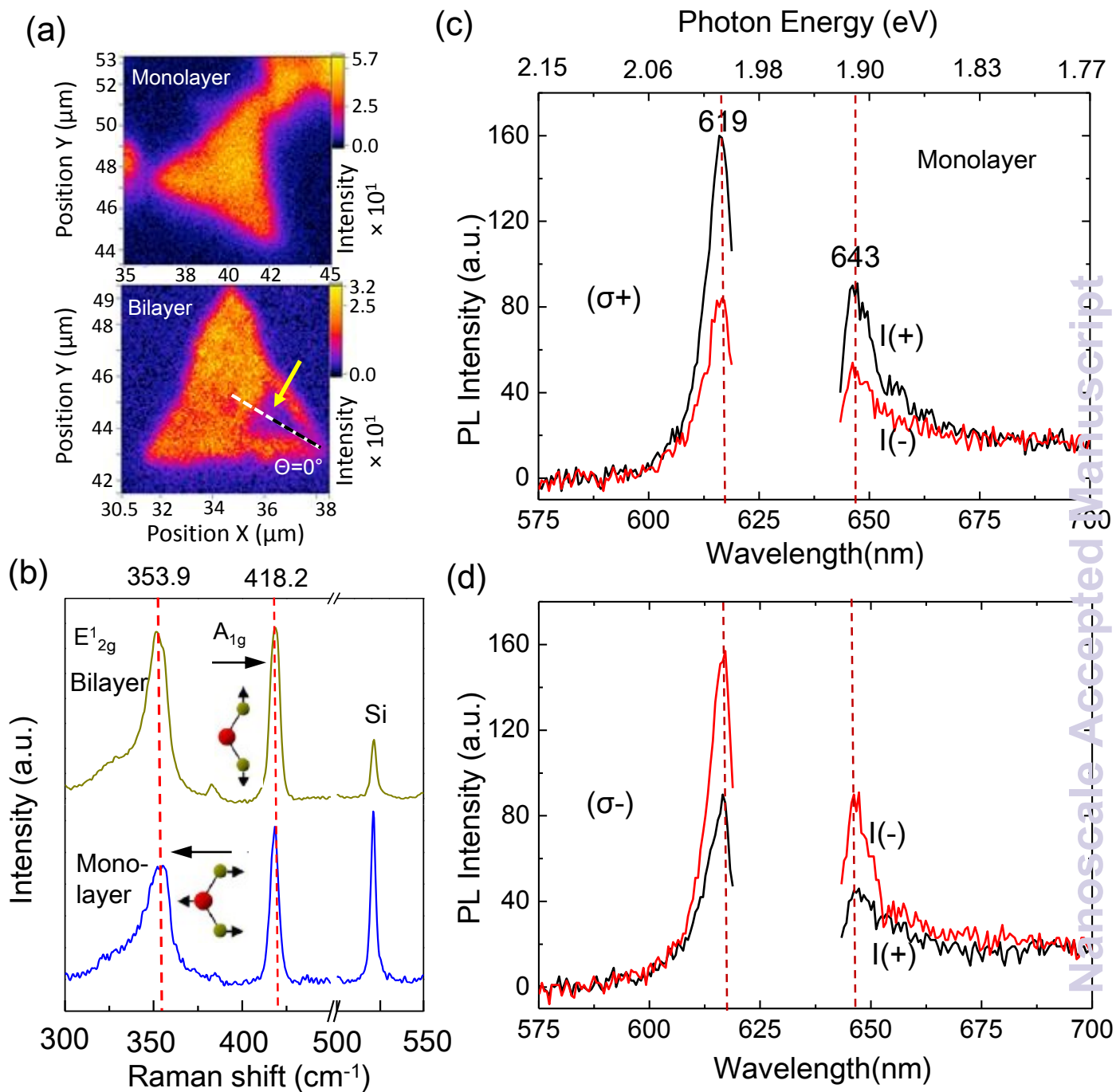
Figure 2 P. K. Nayak *et al.*

(a)

Photon Energy (eV)

(b)
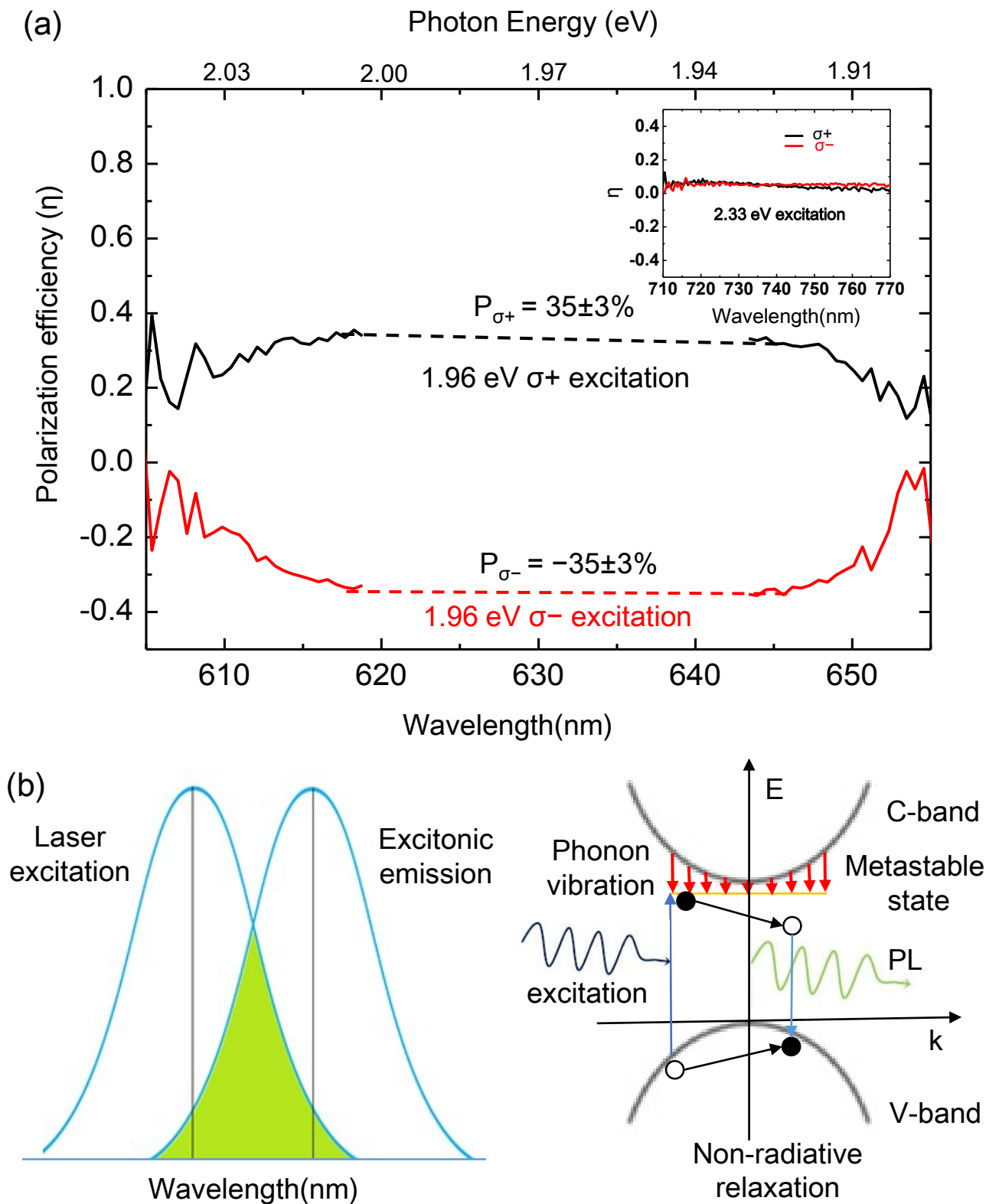
Figure 3 P. K. Nayak *et al.*
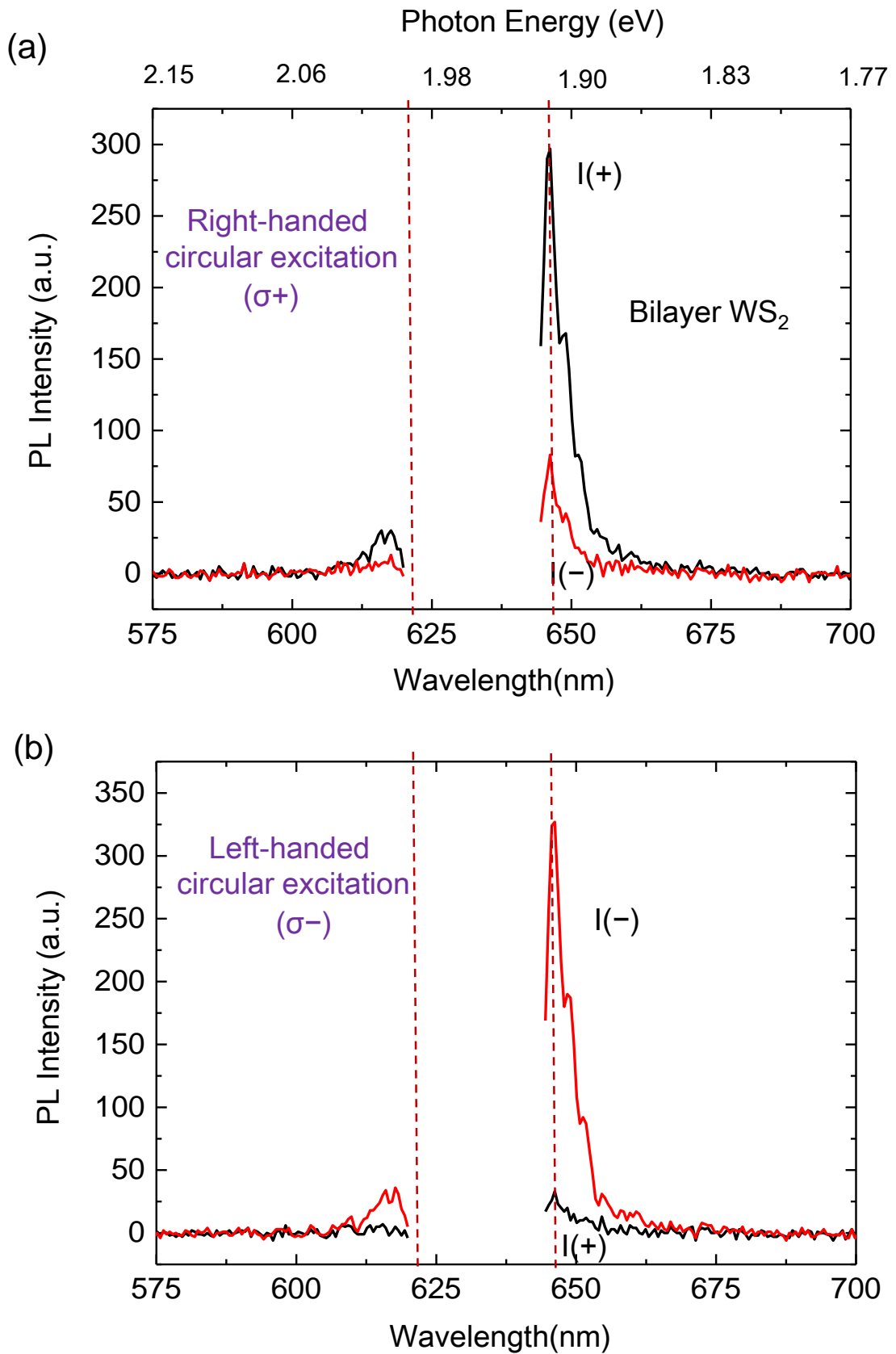
Figure 4 P. K. Nayak *et al.*

(a)

(b)

Figure 5 P. K. Nayak *et al.*